Journal of Materials Chemistry A

PAPER

View Article Online
View Journal | View Issue

Cite this: J. Mater. Chem. A, 2015, 3, 19346

# Targeted synthesis of core–shell porous aromatic frameworks for selective detection of nitro aromatic explosives *via* fluorescence two-dimensional response†

Heping Ma,[a] Bin Li,*[a] Liming Zhang,[a] Dong Han[a] and Guangshan Zhu[b]

A series of core–shell porous aromatic frameworks (PAFs) are synthesized for selective detection of nitro-explosives. The conjugated core–shell PAFs possess large surface areas, which can facilitate the pre-concentration of a targeted analyte, leading to superior sensitivity. The tunable LUMO energy levels of these core–shell PAFs make them selectively detect high explosive TNT and TNP from other competing nitro compounds. Moreover, vapor phase detection of nitro aromatics using $PP_C$-$PPy_S$-PAF-2 exhibits a two dimensional fluorescence signal response toward different nitro aromatics. The power to accurately recognize nitro aromatic explosives in the fluorescent 2D map highlights the core–shell PAFs as very promising materials for nitro explosive sensing.

Received 17th July 2015
Accepted 17th August 2015

DOI: 10.1039/c5ta05447h

www.rsc.org/MaterialsA

## 1. Introduction

Detection of life-threatening explosives is crucial for military endeavors, national security, criminal investigations as well as for the environment and human health.[1] Recent rise in global terrorism requires sensitive, low-cost and miniaturized methods for detecting explosives. Fluorescence sensing has emerged as a desirable approach for many sensing applications because of its potential for high sensitivity, rapidity of analysis, portability, and cost-effectiveness.[2] Utilizing luminescent materials, effective detection of many high explosive or explosive-like molecules can be achieved by changing their optical signals.[3] Numerous electron-rich fluorescent conjugated polymers,[4] dyes,[5] fluorescent organic cages,[6] quantum dots[7] and metal organic frameworks (MOFs)[8] have been used in the detection of trace amounts of nitro aromatics, which are typically based on fluorescence quenching.

However, solely monitoring the change in the emission intensity of luminescent materials can only identify analytes of different categories. For instance, electron deficient molecules as a group can act as fluorescent quenchers. It is still insufficient for accurate and selective detection of one specific electron deficient molecule in their mixture. Upon introducing the change of emission wavelength into the detection map, it can add a new variable of fluorescence signal transduction: from one-dimension (emission intensity) to two-dimensions (both fluorescence intensity and wavelength), which may be an effective method to identify one specific molecule in the presence of others.[9] The pioneering work of Li *et al.* has demonstrated the potential application of luminescent MOFs for the detection of explosives by the fluorescence two-dimensional map.[9,10] Strong analyte–MOF framework interactions are essential to generate a fluorescence signal change both in fluorescence intensity and wavelength. However, the moisture sensitive nature of these MOFs may hinder them in practical applications.

Porous aromatic frameworks (PAFs), as a new class of nanopore materials, have been demonstrated as a frontier research theme in porous materials. The versatile organic moieties in PAFs make them considerable promising materials in gas adsorption,[11] sensing,[12] photoconductive devices[13] and heterogeneous catalysis,[14] *etc.* Conjugated PAFs are attractive materials with π-conjugation properties that allow for the detection of various chemicals. Several porous luminescent PAFs have exhibited fast detection of nitroaromatic explosives *via* fluorescence quenching.[15] Due to the insufficient excitation-emission centers in the skeleton, it is difficult to realize fluorescence two-dimensional (2D) detection in these PAFs. Herein we report the first example of conjugated core–shell porous aromatic frameworks (PAFs) to achieve fluorescence 2D detection of nitroaromatic explosives. The core–shell PAFs possess: (1) large surface areas, which can facilitate the pre-concentration of a targeted analyte, leading to superior sensitivity; (2) two different chromophores in the core and the shell respectively, which can realize both fluorescence intensity and wavelength change in the nitro aromatic explosive detection.

[a]State Key Laboratory of Luminescence and Applications, Changchun Institute of Optics Fine Mechanics and Physics, Chinese Academy of Sciences, Changchun 130033, PR China. E-mail: lib020@ciomp.ac.cn

[b]Faculty of Chemistry, Northeast Normal University, Changchun 130024, PR China

† Electronic supplementary information (ESI) available. See DOI: 10.1039/c5ta05447h

# 2. Results

## 2.1. Synthesis and characterization of PAFs

We employed a blue emitting polyphenylene PAF (PP-PAF) as a core and a polypyrene PAF (PPy-PAF) as a shell to construct core–shell PAFs. The synthetic scheme for this core–shell PAF networks is shown in Fig. 1. The PP-PAF core was synthesized by the Suzuki cross-coupling reaction of benzene-1,4-diboronic acid (BDBA) with 1,3,5-tris(4-bromophenyl)benzene (TBrPB). We used an excess amount of BDBA during core synthesis, which endcapped the core exterior surface of phenylboronic acid functionalities. Phenylboronic acid groups were then reacted with 1,3,6,8-tetrabromopyrene (TBrPy) for shell formation, which ensured shell growth on the exterior surface of the core.[16] Changing the TBrPB/TBrPy molar ratio from 8 to 4 and 2 yielded PAFs with three different core–shell compositions named: $PP_C$-$PPy_S$-PAF-1, $PP_C$-$PPy_S$-PAF-2 and $PP_C$-$PPy_S$-PAF-3, respectively. As a comparison, we also prepared the PP-PAF and PPy-PAF, with TBrPB/TBrPy and BDBA at a molar ratio of 3 : 1, respectively.

All above mentioned polymers were insoluble in common organic solvents such as DMF, THF, methanol, DMSO and water. As found for other phenyl connected porous organic frameworks,[17] these PAFs were also chemically stable: for example, $PP_C$-$PPy_S$-PAFs kept their skeleton unchanged even in aqueous solutions of 3 M HCl and NaOH for one week.

The PAF samples are first studied by FT-IR spectroscopy and solid-state $^{13}C$ cross-polarization magic-angle spinning (CP/MAS) NMR. The IR spectra of the as-prepared PAFs and their starting monomers are shown in Fig. 2. The IR bands corresponding to stretching vibrations of the B–O group (1342 $cm^{-1}$) in the PP-PAF core are similar to those of its monomer BDBA, which means that B–O groups cover the core. The disappearance of signal assigned to B–O units in all core–shell PAFs demonstrates that the core is covalently covered by the shell. Meanwhile, the IR bands related to C–Br vibration mode at 1072 $cm^{-1}$ and 507 $cm^{-1}$ in the TBrPy monomer vanish into the background in all core–shell PAFs, which gives a distinct proof for the complete reaction between the core and shell. PP-PAF and $PP_C$-$PPy_S$-PAF-2 were further characterized by solid-state $^{13}C$ CP/MAS NMR (Fig. S1†). The broad peaks at approximately 147 ppm and 133 ppm are detected, corresponding to substituted aromatic carbon and non-substituted aromatic carbon respectively, which indicates that both PAF frameworks are composed of highly conjugated aromatic groups. A NMR signal around 127.1 ppm (assigned to the carbon atom in aromatic boronic acid) is observed in the PP-PAF, which indicates that the PP-PAF core is covered by C–B units. Thermal stability of the PAFs is studied by TGA (Fig. S2†). A distinct weight loss in the range of 300–400 °C is observed, which corresponds to the decomposition or collapse of the organic skeleton. X-ray photoelectron spectroscopy (XPS) was utilized to determine the purity of our product. The XPS spectra of $PP_C$-$PPy_S$-PAF-2 are shown in Fig. S3.† As can be seen, the main element observed in the

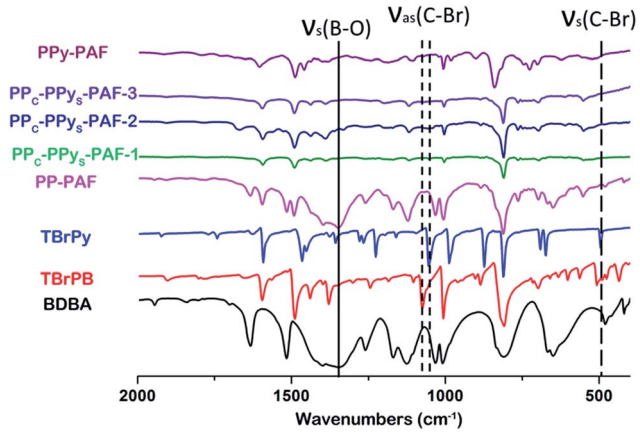


Fig. 2 FT-IR spectra of starting monomers and the as-prepared PAFs.

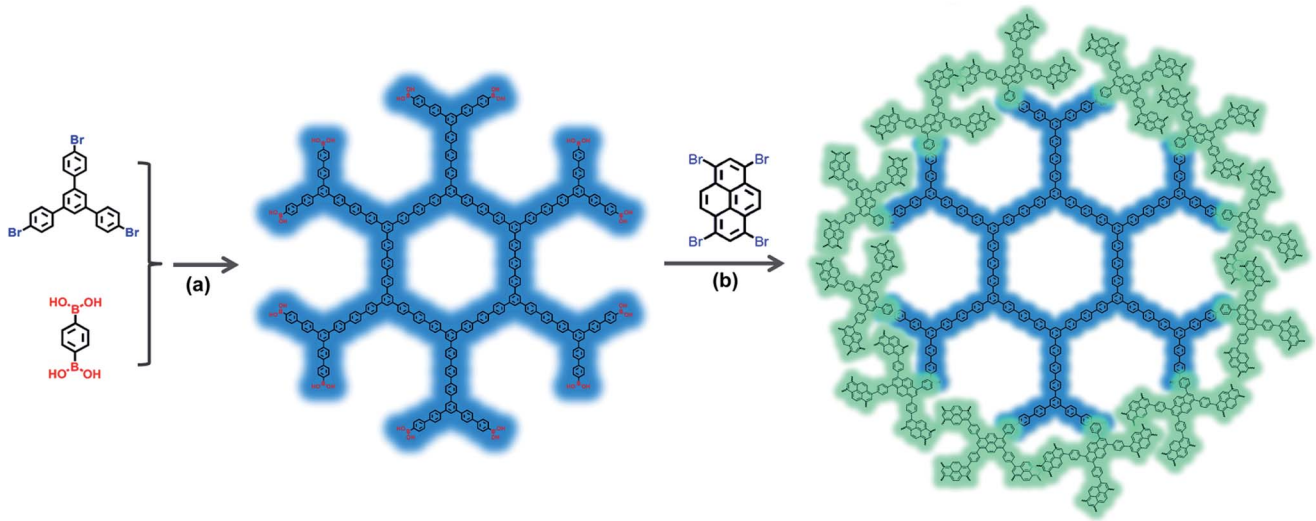


Fig. 1 Schematic representation of the synthesis of core–shell PAFs. (a) $K_2CO_3$ and $Pd(PPh_3)_4$ in DMF, 90 °C, 12 h; (b) $K_2CO_3$ and $Pd(PPh_3)_4$ in DMF, 120 °C, 2 d.

polymer network is the C element. The low signals from Br, Pd, and N in magnified views of XPS spectra indicate that trace residues of monomers, catalysts, and DMF in the final sample. Powder X-ray diffraction (PXRD) measurements indicate that all PAFs are amorphous (Fig. S4†). Scanning electron microscopy (SEM) shows that as pyrene shell grows, the particle sizes are increased (Fig. S5†).

### 2.2. Porosity of PAFs

The porosity of these PAFs was investigated by nitrogen adsorption and desorption measurements at 77 K. As shown in Fig. 3, a sharp increase in the gas uptake is observed at low pressure in adsorption–desorption isotherms of the PP-PAF, which confirms the existence of micropores in the PAF. The Brunauer–Emmett–Teller (BET) surface area of the PP-PAF is 265 $m^2 g^{-1}$. A weak hysteretic shoulder in desorption isotherms of $PP_C$-$PPy_S$-PAFs prove that these core–shell materials feature a small degree of mesoporosity. The BET surface area is increasing as the shell thickness increases. $PP_C$-$PPy_S$-PAF-1 has a BET surface area of 388 $m^2 g^{-1}$, while BET surface areas are increased to 402 and 415 $m^2 g^{-1}$ for $PP_C$-$PPy_S$-PAF-2 and $PP_C$-$PPy_S$-PAF-3, respectively.

### 2.3. Photophysical property

The solid UV-visible absorption spectra were used to monitor how the π-conjugated network developed during the shell growth. As shown in Fig. 4 and S6b,† the PP-PAF core exhibits an absorption band at 400 nm. The $PP_C$-$PPy_S$-PAF-1 sample exhibits a red-shifted absorption band at 458 nm. As the $PPy_S$-PAF shell network becomes thicker, the absorption bands are further red-shifted to 460 and 470 nm for $PP_C$-$PPy_S$-PAF-2 and $PP_C$-$PPy_S$-PAF-3, respectively. These data show that it is possible to tune the optical band gaps of core–shell porous networks by adjusting the core–shell ratio.

Photoluminescence spectra of these PAFs in ethanol solution are given in Fig. 5a, while excitation spectra are shown as Fig. S6a.† Upon excitation of 310 nm in EtOH, the PP-PAF core

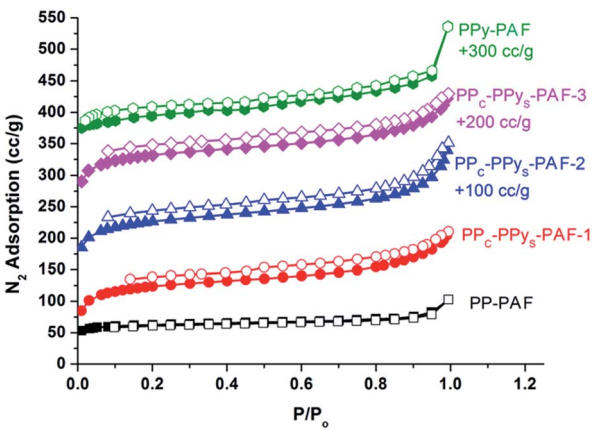


Fig. 3 $N_2$ adsorption/desorption isotherms of the PAFs measured at 77 K; the adsorption branch is denoted by closed symbols, and desorption branch by open symbols.

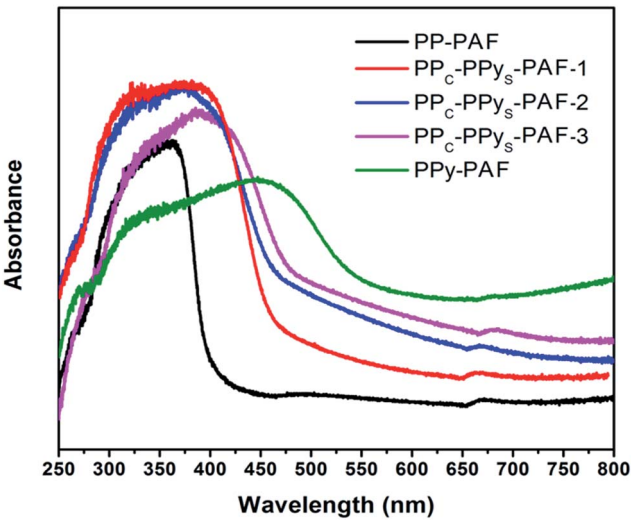


Fig. 4 UV-visible absorption spectra of the PAFs measured in the solid state.

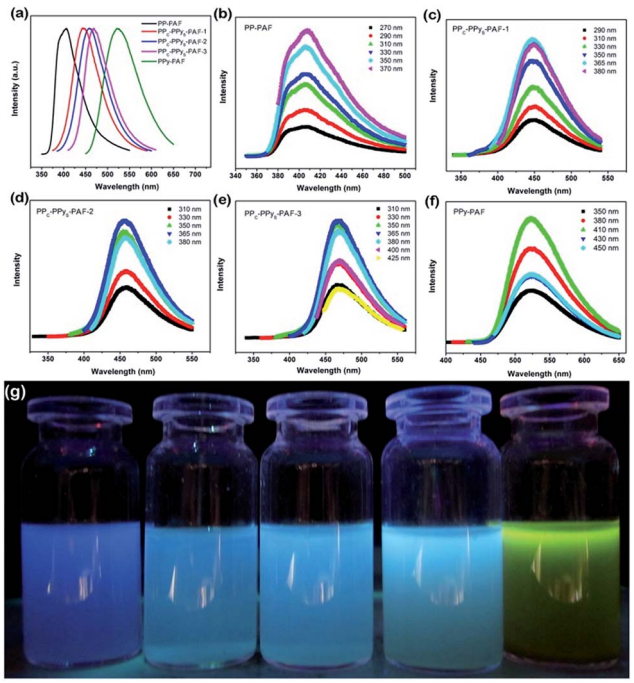


Fig. 5 (a) Photoluminescence spectra of the PAFs measured in ethanol. A redshift is observed as the pyrene shell incorporation is increased; (b–f) the excitation-independent PL behavior of PAFs; (g) photographs of suspensions of the PAFs in ethanol (5 mg/10 mL) imaged under irradiation with UV light (λ excitation = 365 nm).

emits a deep-blue luminescence at 409 nm. The PPy-PAF exhibits a 525 nm emission upon excitation of 365 nm. As the pyrene shell becomes thicker, a red shift emission is observed, which indicates the extended π-electronic conjugation over the PAF skeleton. $PP_C$-$PPy_S$-PAF-1 shows an emission maximum at 452 nm, while $PP_C$-$PPy_S$-PAF-2 gives a luminescence centered at 455 nm. The emission band is further red-shifted to 459 nm for $PP_C$-$PPy_S$-PAF-3. Moreover, PL maxima of $PP_C$-$PPy_S$-PAFs are well

 

confined and independent of the excitation wavelength (Fig. 5b–f). We also investigated the PL quantum yield (QY) variation of core–shell PAFs (Table S1†). The PP-PAF shows an absolute QY of 0.1. $PP_C$-$PPy_S$-PAF-1 with a thin shell exhibits a QY value (0.1) similar to that of the PP-PAF core. As the shell became thicker, $PP_C$-$PPy_S$-PAFs show enhanced luminescence: the QYs for $PP_C$-$PPy_S$-PAF-2 and $PP_C$-$PPy_S$-PAF-3 are 0.13 and 0.17, respectively.

### 2.4. Fluorescence response of nitro aromatics in solution

High PL performance and the porous nature of the PAFs inspire us to evaluate their nitro aromatic detection properties. *p*-Nitrotoluene (NT), 4-chloro-nitrobenzene (Cl-NB), 2,4-dinitrotoluene (DNT), 2,4,6-trinitrotoluene (TNT) and 2,4,6-trinitrophenol (TNP) are selected as probe molecules to assess the nitroaromatic compound detection properties of the PAFs. We first evaluated the fluorescence response of these PAFs to nitro aromatics in solution. Fluorescence quenching titrations of different nitro aromatics were performed by adding various analytes to ethanol solutions of PAFs. The PL quenching behavior of these PAFs upon addition of various concentrations of NT, TNP, is shown in Fig. 6. Other titration plots can be found in the ESI (Fig. S7–S11†). Immediate fluorescence quenching was observed upon adding high explosive nitro aromatic molecules (TNT and TNP). For the PP-PAF, its luminescence intensity is largely dependent on the concentration of nitro aromatic explosives. Moreover, quenching degrees of samples with the same PAF structure for different nitro aromatics are clearly different. The ability of quenching efficiency is in accordance with their order of electron deficiency, where electron withdrawing ability of nitro groups present in the nitro aromatics generally follow the order: TNP > TNT > DNT > Cl-NB > NT. For $PP_C$-$PPy_S$-PAF-1, $PP_C$-$PPy_S$-PAF-2 and $PP_C$-$PPy_S$-PAF-3, the core–shell composition demonstrates a considerably better selectivity towards TNP and TNT compared to that of the PP-PAF and PPy-PAF (Fig. 6k–o). Taking $PP_C$-$PPy_S$-PAF-2 for example, $PP_C$-$PPy_S$-PAF-2 shows very little quenching for Cl-NB, and NT at a concentration of 50 ppm. The emission peak intensity of $PP_C$-$PPy_S$-PAF-2 is decreased by 8% and 7% for Cl-NB and NT, respectively. While $PP_C$-$PPy_S$-PAF-2 shows 58% quenching after adding TNT and 62% quenching after adding TNP at the same concentration, respectively. The quenching efficiency was analyzed using the Stern–Volmer equation: $(F_0/F) = K_{sv}[Q] + 1$, where $F_0$ and $F$ are the fluorescence intensities before and after addition of the analyte, respectively, $K_{sv}$ is the quenching constant ($ppm^{-1}$), and [Q] is the concentration of the analyte. The SV plots for NB, 2-NT, TNT, and TNP were nearly linear at low concentrations (<75 ppm), and subsequently deviated from linearity. The calculated $K_{sv}$ values for TNT and TNP were $2.21 \times 10^{-2}$ $ppm^{-1}$ and $2.42 \times 10^{-2}$ $ppm^{-1}$, respectively, which are greater than Cl-NB ($3.17 \times 10^{-3}$ $ppm^{-1}$) and NT ($2.33 \times 10^{-3}$ $ppm^{-1}$). The most analogous quenching efficiency was also observed for $PP_C$-$PPy_S$-PAF-1 and $PP_C$-$PPy_S$-PAF-3. For the pyrene rich PPy-PAF, upon addition of the same amount of nitro

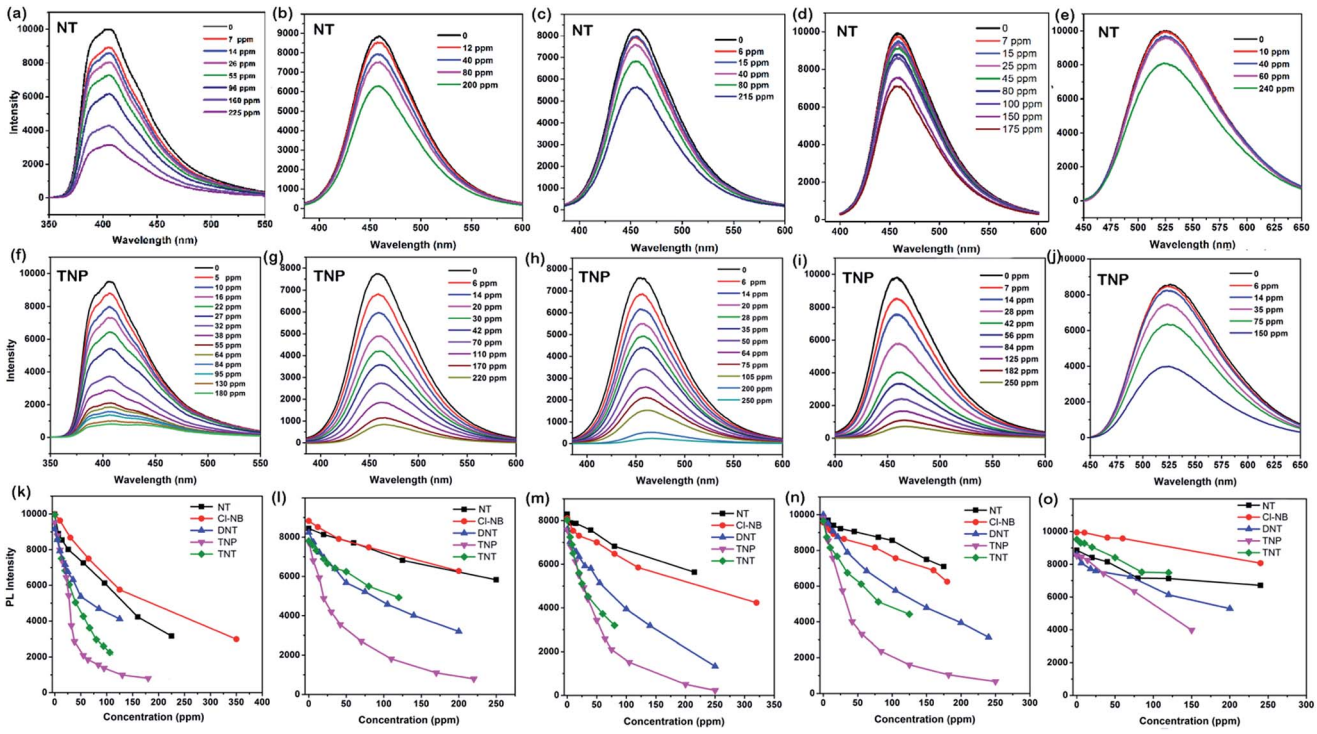


Fig. 6 (a–e) Effect on the emission spectra of PAFs dispersed in ethanol upon incremental addition of a NT solution, (a) for PP-PAF, (b) for $PP_C$-$PPy_S$-PAF-1, (c) for $PP_C$-$PPy_S$-PAF-2, (d) for $PP_C$-$PPy_S$-PAF-3, (e) for PPy-PAF; (f–j) effect on the emission spectra of PAFs dispersed in ethanol upon incremental addition of a TNP solution, (f) for PP-PAF, (g) for $PP_C$-$PPy_S$-PAF-1, (h) for $PP_C$-$PPy_S$-PAF-2, (i) for $PP_C$-$PPy_S$-PAF-3, (j) for PPy-PAF; (k–o) decrease in PAF fluorescence intensity upon the addition of ethanol solutions of different nitro compounds, (k) for PP-PAF, (l) for $PP_C$-$PPy_S$-PAF-1, (m) for $PP_C$-$PPy_S$-PAF-2, (n) for $PP_C$-$PPy_S$-PAF-3, (o) for PPy-PAF.

aromatic compounds, a little effect on fluorescence intensity variation was observed.

To understand the origin of $PP_C$-$PPy_S$-PAF-2 high selectivity towards high explosive TNT and TNP, the mechanism of quenching was investigated. Generally, the fluorescence quenching phenomenon can be explained by the donor–acceptor electron-transfer mechanism through the interaction between electron-rich PAFs and electron-deficient analytes.[18] The PAFs can be regarded as giant molecules. Similarly their valence and conduction bands can be treated similar to molecular orbitals (MOs). Upon excitation, an effective electron transfer occurs from the PAF's LUMO to the analyte's LUMO only if the electron-deficient analyte's LUMO lies between the LUMO and HOMO levels of the electron-rich PAFs. Therefore, for electron-deficient analytes with stabilized LUMOs, the PAF usually owns a higher LUMO energy level, electron transfer between them becomes thermodynamically favorable, which may result in a high quenching efficiency. If the LUMO of the analyte is higher than that of the PAF, an effective electron transfer will not occur. The corresponding PL quenching phenomenon will not be obvious. We use cyclic voltammetry (CV) measurements and absorption spectra to evaluate the HOMO and LUMO changing of these core–shell PAFs compared to the PP-PAF. The onset potential of oxidation for the PP-PAF is +1.17 V *vs.* a saturated calomel electrode (SCE) (see Fig. S12 in ESI†). Hence, the PP-PAF's HOMO level is estimated to be −5.91 eV. With the increase of the pyrene content in the shell, the onset potential of oxidation for $PP_C$-$PPy_S$-PAFs correspondingly increases (Fig. S12 and Table S1†). The LUMO levels are determined by combining their CV oxidation potentials with their optical energy band gaps. As shown in Fig. S6b,† $PP_C$-$PPy_S$-PAFs exhibit redshift in the UV-visible spectra compared with the PP-PAF. The estimated LUMO energy levels of core–shell PAFs are lower than that of the PP-PAF (Table S1†). This result is consistent with time-dependent density functional theory (TD-DFT) calculations reported previously.[19]

Fig. 7 shows the HOMO and LUMO energy levels of these PAFs and electron-deficient nitro compounds as calculated by density functional theory at the B3LYP/6-31G* level (see the ESI and Table S2†). The LUMO of the PP-PAF is higher than those of all the nitro compounds and thus maintains a better driving force for electron transfer to electron-deficient analytes. So fluorescence quenching was observed for all compounds. Along with the increase of pyrene moieties in the shell, the LUMOs of these $PP_C$-$PPy_S$-PAFs decreased. Since the LUMO energy level of $PP_C$-$PPy_S$-PAF-2 is lower than those of Cl-NB and NT, the observed quenching efficiency of the $PP_C$-$PPy_S$-PAF for Cl-NB and NT is inconspicuous. Thus, $PP_C$-$PPy_S$-PAF-2 exhibits selective detection for high explosive TNT and TNP from other nitro aromatics.

The high quenching efficiency of the $PP_C$-$PPy_S$-PAF for TNT in solution (Fig. 8a) drives us to testify their selective detection of TNP and TNT for practical applications. We dope $PP_C$-$PPy_S$-PAF-2 into portable paper-based test strips, which allows a simple and low cost protocol for on-site instant detection. As a comparison, we also dope PP-PAF into a strip in the same way (the detailed method of making test strips is described in the ESI†). The resulting test strips display deep-blue photoluminescence (410 nm) for the PP-PAF and sky-blue photoluminescence (455 nm) for $PP_C$-$PPy_S$-PAF-2 upon exposure to a standard handheld UV (365 nm) lamp, respectively (Fig. 8b). To test the sensitivity of these test strips to TNT, different concentrations of TNT solutions (0.25, 5, 10, 15, 20 and 25 mM) were spotted onto the prepared $PP_C$-$PPy_S$-PAF-2 strip. The photographs of these test strips after spotted by TNT are shown in Fig. 8c. There was a visible difference in the quenched spots for the different concentrations of TNT. To further test the application of the $PP_C$-$PPy_S$-PAF-2 test strip for selective detection of TNP and TNT, we use 100 ppm nitroaromatic compounds in ethanol solution as an ink and write in the PP-PAF and $PP_C$-$PPy_S$-PAF-2 strips. As shown in Fig. 8d, for the PP-PAF test strip, when 100 ppm solutions of NT, Cl-NB, DNT, TNT

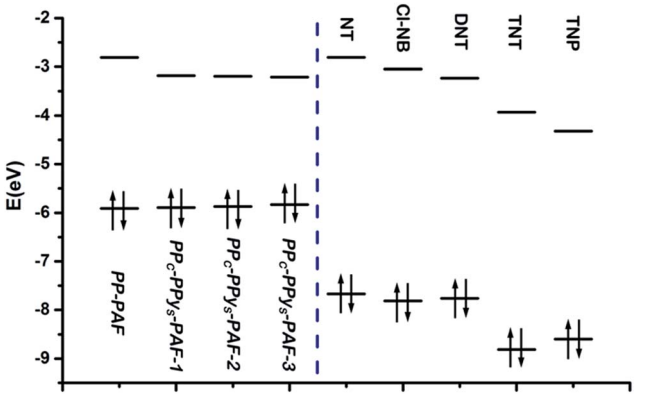


Fig. 7 HOMO and LUMO energies for PAFs and analytes arranged in descending order of LUMO energies.

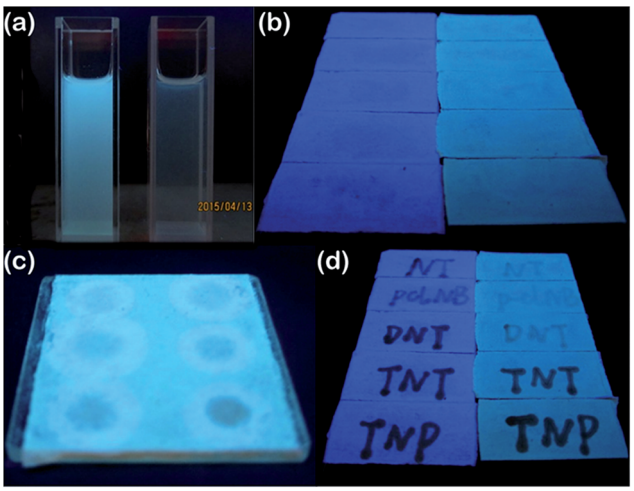


Fig. 8 (a) Photographs of the original fluorescence and the decreased fluorescence upon addition of TNT in ethanol; (b) photographs of the PP-PAF and $PP_C$-$PPy_S$-PAF-2 test strips under UV light; (c) photographs of $PP_C$-$PPy_S$-PAF-2 test strips after spotting ethanol solution of TNT at different concentrations; (d) photographs of the PP-PAF and $PP_C$-$PPy_S$-PAF-2 test strips under UV light after writing with 100 ppm solutions of NT, Cl-NB, DNT, TNT and TNP.

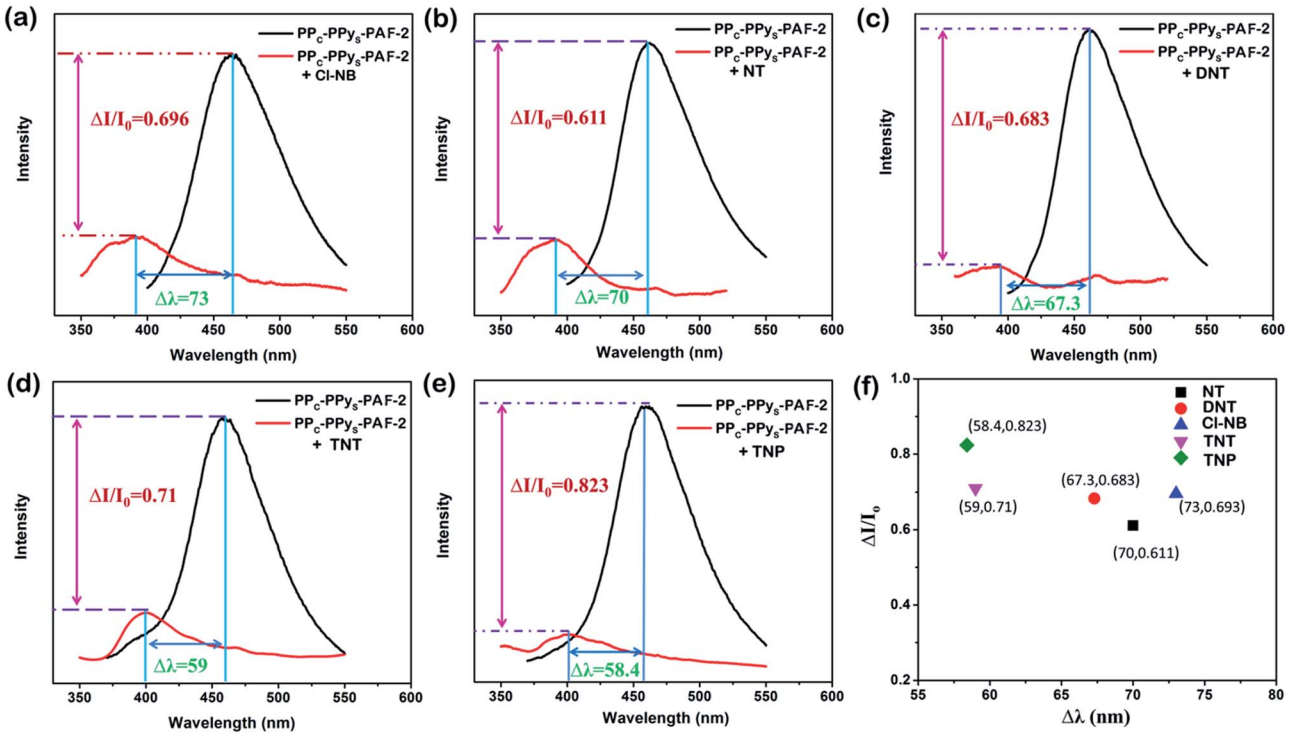


Fig. 9 Emission spectra of $PP_C$-$PPy_S$-PAF-2 before (black) and after (red) upon exposure to (a) Cl-NB, (b) NT, (c) DNT, (d) TNT and (e) TNP vapor at room temperature; (f) a 2D color coded map of nitro aromatics based on the fluorescence response of $PP_C$-$PPy_S$-PAF-2.

and TNP were written onto the strip, its fluorescence was rapidly and almost completely quenched for all compounds. While for the $PP_C$-$PPy_S$-PAF-2 test strip, only high explosive TNT and TNP quenched the test strip completely. This result showed that the $PP_C$-$PPy_S$-PAF-2 test strip is highly sensitive to explosive TNT and TNP with good selectivity.

### 2.5. Fluorescence response to nitro aromatic vapors

For practical applications, we further explore $PP_C$-$PPy_S$-PAF for detecting nitro aromatics in the vapor phase. The thick and dense test strips show slow (>5 min) and unspectacular fluorescence quenching response to nitro aromatics (Fig. S13†). A thin layer of $PP_C$-$PPy_S$-PAF-2 was prepared using the method reported by Li *et al.*[8a] As shown in Fig. 9a–e, fast fluorescence response was observed after exposing $PPy_S$-PAF-2 towards nitro-compound vapor for 2 min. Along with the reduction of emission at 455 nm, we also monitor a weak emission around 400 nm for $PP_C$-$PPy_S$-PAF-2, which is very similar to the PP-PAF core. Utilizing both the fluorescence intensity change and emission wavelength shift of $PP_C$-$PPy_S$-PAF-2, we can realize fluorescence 2D detection for these nitro-compounds. The fluorescence intensity change and emission wavelength shift of $PP_C$-$PPy_S$-PAF-2 for different nitro aromatics are plotted in Fig. 9f. These nitro-compounds are well spread on the 2D map and can be uniquely identified. In vapor detection, the nitro compounds only adsorbed on the PAF surface, the emission of the pyrene shell was quenched effectively. Since the shell layer of $PP_C$-$PPy_S$-PAF-2 is very thin, the emission of the PP-PAF core can be transmitted through the shell and be detected. This result represents a promising demonstration of nitro aromatic vapor fluorescence 2D detection using the core–shell structured PAF. Future studies will focus on preparing a novel core–shell PAF so as to increase fluorescence 2D selectivity and sensitivity toward specific class of explosives.

## 3. Conclusions

In conclusion, we have designed and synthesized a series of core–shell conjugated porous aromatic frameworks as fluorescent sensors for the detection of nitro aromatic explosives. The core–shell PAFs exhibited selective detection of high explosive TNT and TNP, over other nitro compounds. Their selectivity can be explained by the decrease of the LUMO energy level of the $PP_C$-$PPy_S$-PAF after introducing the pyrene moiety into the shell. Moreover, vapor phase detection of nitro-aromatic compounds for $PP_C$-$PPy_S$-PAF-2 demonstrated that the core–shell strategy could achieve fluorescence 2D detection of nitro aromatics. Additionally, because the richness of organic building block could be used to tune their LUMO energy levels in the core–shell PAF platform, this very promising approach should be of practical potential for sensitizing and probing different substrate molecules by tuning HOMO–LUMO energy levels. The power to unambiguously recognize nitro aromatic explosives in the fluorescent 2D map highlighted this approach as a very promising strategy to develop luminescent core–shell PAFs with unprecedented potential applications.

# 4. Experimental section

### 4.1. Synthesis of PP-PAF

A mixture of 1,3,5-tris(4-bromophenyl)benzene (TBrPB) (100 mg, 0.185 mmol), and benzene-1,4-diboronic acid (BDBA) (92 mg, 0.555 mmol) in DMF (15 mL) was degassed by three freeze–pump–thaw cycles. To the mixture was added an aqueous solution of $K_2CO_3$ (2.0 M, 1.0 mL) and $Pd(PPh_3)_4$ (15.0 mg). The mixture was degassed by three freeze–pump–thaw cycles, and purged with $N_2$, and stirred at 90 °C for 20 h. The precipitate was filtered, washed with water, methanol, THF, and DMF. Further purification was carried out by Soxhlet extraction with methanol and THF for 48 h, respectively. After drying in a vacuum oven at 150 °C, PP-PAF was obtained as a grey solid in 85% yield.

### 4.2. Synthesis of $PP_C$-$PPy_S$-PAF-1

A mixture of 1,3,5-tris(4-bromophenyl)benzene (TBrPB) (100 mg, 0.185 mmol), and benzene-1,4-diboronic acid (BDBA) (92 mg, 0.555 mmol) in DMF (15 mL) was degassed by three freeze–pump–thaw cycles. To the mixture was added an aqueous solution of $K_2CO_3$ (2.0 M, 1.0 mL) and $Pd(PPh_3)_4$ (15.0 mg). The mixture was degassed by three freeze–pump–thaw cycles, and purged with $N_2$, and stirred at 90 °C for 12 h. The mixture was allowed to cool at room temperature, and was added with a mixture of 1,3,6,8-tetrabromopyrene (0.023 mmol, 12 mg) and catalyst (2 M $K_2CO_3$, 0.4 mL and $Pd(PPh_3)_4$ 9 mg). The resulting mixture was degassed by three freeze–pump–thaw cycles purged with $N_2$, and stirred at 120 °C for 2 days. The precipitate was filtered, washed with water, methanol, THF, and DMF. Further purification was carried out by Soxhlet extraction with methanol and THF for 48 h, respectively. After drying in a vacuum oven at 150 °C, $PP_C$-$PPy_S$-PAF-1 was obtained as a grey solid in 87% yield.

For the synthesis of $PP_C$-$PPy_S$-PAF-2 and $PP_C$-$PPy_S$-PAF-3, the same reaction procedure was performed except for adding 0.046 mmol and 0.092 mmol of 1,3,6,8-tetrabromopyrene respectively.

# Acknowledgements

The authors gratefully thank the financial support of the NSFC (Grant No. 21501166, 51172224 and 51372240).

# Notes and references

1 (*a*) S. W. Thomas III, G. D. Joly and T. M. Swager, *Chem. Soc. Rev.*, 2007, **36**, 1339; (*b*) R. L. Woodfin, *Trace Chemical Sensing of Explosives*, John Wiley & Sons, 2006.

2 R. A. Agbaria, P. B. Oldham, M. McCarroll, L. B. McGown and I. M. Warner, *Anal. Chem.*, 2002, **74**, 3952.

3 Y. Salinas, R. Martinez-Manez, M. D. Marcos, F. Sancenon, A. M. Castero, M. Parra and S. Gil, *Chem. Soc. Rev.*, 2012, **41**, 1261.

4 (*a*) M. E. Germain and M. J. Knapp, *Chem. Soc. Rev.*, 2009, **38**, 2543; (*b*) S. W. Thomas, G. D. Joly and T. M. Swager, *Chem. Rev.*, 2007, **107**, 1339.

5 N. Venkatramaiah, A. Firmino, F. A. Almeida Paz and J. P. C. Tomé, *Chem. Commun.*, 2014, **50**, 9683.

6 K. Acharyya and P. Sarathi Mukherjee, *Chem. Commun.*, 2014, **50**, 15788.

7 (*a*) K. Zhang, H. Zhou, Q. Mei, S. Wang, G. Guan, R. Liu, J. Zhang and Z. Zhang, *J. Am. Chem. Soc.*, 2011, **133**, 8424; (*b*) R. Freeman, T. Finder, L. Bahshi, R. Gill and I. Willner, *Adv. Mater.*, 2012, **24**, 6416; (*c*) P. Wu, C. Xu, X. Hou, J. Xu and H. Chen, *Chem. Sci.*, 2015, **6**, 4445–4450.

8 (*a*) A. Lan, K. Li, H. Wu, D. H. Olson, T. J. Emge, W. Ki, M. Hong and J. Li, *Angew. Chem., Int. Ed.*, 2009, **48**, 2334; (*b*) S. S. Nagarkar, B. Joarder, A. K. Chaudhari, S. Mukherjee and S. K. Ghosh, *Angew. Chem., Int. Ed.*, 2013, **52**, 2881; (*c*) B. Gole, A. K. Bar and P. S. Mukherjee, *Chem.–Eur. J.*, 2014, **20**, 13321; (*d*) H. Xu, F. Liu, Y. Cui, B. Chen and G. Qian, *Chem. Commun.*, 2011, **47**, 3153; (*e*) S. S. Nagarkar, A. V. Desai and S. K. Ghosh, *Chem. Commun.*, 2014, **50**, 8915; (*f*) J. Qin, B. Ma, X.-F. Liu, H.-L. Lu, X.-Y. Dong, S.-Q. Zang and H. Hou, *J. Mater. Chem. A*, 2015, **3**, 12690.

9 Z. Hu, B. J. Deibert and J. Li, *Chem. Soc. Rev.*, 2014, **43**, 5815.

10 (*a*) Z. Hu, S. Pramanik, K. Tan, C. Zheng, W. Liu, X. Zhang, Y. J. Chabal and J. Li, *Cryst. Growth Des.*, 2013, **13**, 4204; (*b*) Z. Hu, K. Tan, W. P. Lustig, H. Wang, Y. Zhao, C. Zheng, D. Banerjee, T. J. Emge, Y. J. Chabal and J. Li, *Chem. Sci.*, 2014, **5**, 4873.

11 (*a*) R. Dawson, A. I. Cooper and D. J. Adams, *Prog. Polym. Sci.*, 2012, **37**, 530; (*b*) X. Q. Zou, H. Ren and G. S. Zhu, *Chem. Commun.*, 2013, **49**, 3911.

12 (*a*) X. Liu, Y. Xu and D. Jiang, *J. Am. Chem. Soc.*, 2012, **134**, 8738; (*b*) C. Gu, N. Huang, J. Gao, F. Xu, Y. Xu and D. Jiang, *Angew. Chem., Int. Ed.*, 2014, **53**, 4850.

13 (*a*) L. Chen, Y. Honsho, S. Seki and D. Jiang, *J. Am. Chem. Soc.*, 2010, **132**, 6742; (*b*) K. Zhang, D. Kopetzki, P. H. Seeberger, M. Antonietti and F. Vilela, *Angew. Chem., Int. Ed.*, 2012, **52**, 1432; (*c*) X. Feng, X. Ding and D. Jiang, *Chem. Soc. Rev.*, 2012, **41**, 6010.

14 (*a*) L. Chen, Y. Yang, Z. Guo and D. Jiang, *Adv. Mater.*, 2011, **23**, 3149; (*b*) J. X. Jiang, C. Wang, A. Laybourn, T. Hasell, R. Clowes, Y. Z. Khimyak, J. Xiao, S. J. Higgins, D. J. Adams and A. I. Cooper, *Angew. Chem., Int. Ed.*, 2011, **50**, 1072; (*c*) R. K. Totten, Y.-S. Kim, M. H. Weston, O. K. Farha, J. T. Hupp and S. T. Nguyen, *J. Am. Chem. Soc.*, 2013, **135**, 11720.

15 (*a*) D. Gopalakrishnan and W. R. Dichtel, *J. Am. Chem. Soc.*, 2013, **135**, 8357; (*b*) Y. Yuan, H. Ren, F. Sun, X. Jing, K. Cai, X. Zhao, Y. Wang, Y. Wei and G. Zhu, *J. Phys. Chem. C*, 2012, **116**, 26431; (*c*) N. Sang, C. Zhan and D. Cao, *J. Mater. Chem. A*, 2015, **3**, 92.

16 Y. Xu, A. Nagai and D. Jiang, *Chem. Commun.*, 2013, **49**, 1591.

17 T. Ben, H. Ren, S. Q. Ma, D. P. Cao, J. H. Lan, X. F. Jing, W. C. Wang, J. Xu, F. Deng, J. M. Simmons, S. L. Qiu and G. S. Zhu, *Angew. Chem., Int. Ed.*, 2009, **48**, 9457.

18 D. T. McQuade, A. E. Pullen and T. M. Swager, *Chem. Rev.*, 2000, **100**, 2537.

19 R. S. Sprick, J.-X. Jiang, B. Bonillo, S. Ren, T. Ratvijitvech, P. Guiglion, M. A. Zwijnenburg, D. J. Adams and A. I. Cooper, *J. Am. Chem. Soc.*, 2015, **137**, 3265.

 